

# Enhanced Doxorubicin Delivery in Folate-Overexpressed Breast Cancer Cells Using Mesoporous Carbon Nanospheres

Kandasamy Vinothini, Sathish Sundar Dhilip Kumar, Heidi Abrahamse, and Mariappan Rajan\*

Cite This: *ACS Omega* 2021, 6, 34532–34545

Read Online

ACCESS |



Metrics &amp; More

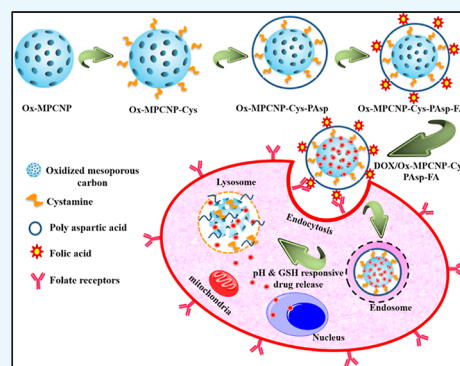


Article Recommendations



Supporting Information

**ABSTRACT:** Nanoparticle-based drug delivery reveals the safety and effectiveness and avoids premature drug release from the nanocarrier. These nanoparticles improve the bioavailability and stability of the drug against chemical and enzymatic degradation and facilitate targeted drug delivery. Herein, targeted folic acid-conjugated oxidized mesoporous carbon nanospheres (Ox-MPCNPs) were successfully fabricated and developed as antitumoral doxorubicin delivery for targeted breast cancer therapy. Fourier transform infrared spectroscopy studies confirmed that the doxorubicin was successfully bound on the Ox-MPCNP through hydrogen bonding and  $\pi-\pi$  interactions. X-ray diffraction studies showed that the synthesized doxorubicin-loaded Ox-MPCNP is semi-crystalline. The surface morphology of the synthesized doxorubicin-loaded Ox-MPCNP (DOX/Ox-MPCNP-Cys-PAsp-FA) was studied by scanning electron microscopy and high-resolution transmission electron microscopy, which demonstrates a sphere-shaped morphology. The cytotoxic effects of DOX/Ox-MPCNP-Cys-PAsp-FA were studied in MCF-7 breast cancer cells using the CytoTox96 assay kit. The study confirmed the cytotoxic effects of the synthesized nanospheres *in vitro*. Moreover, DOX/Ox-MPCNP-Cys-PAsp-FA-treated cells displayed efficient cell apoptosis and cell death in flow cytometry analysis. The mitochondrial fragmentation and nucleus damages were further confirmed by fluorescence microscopy. Thus, the approach used to construct the DOX/Ox-MPCNP-Cys-PAsp-FA carrier provides excellent opportunities for the targeted treatment of breast cancer.



## 1. INTRODUCTION

In recent years, chemotherapy has become an indispensable treatment for cancer patients, so many chemotherapeutic anticancer drugs are used to damage or kill tumor cells. It received significant attention for clinical approaches.<sup>1</sup> The conventional targeted chemotherapeutic drug delivery systems help increase the bioavailability of drugs in affected areas and are expected to be effective for safe, convenient, and biologically important cancer treatments.<sup>2</sup> Various nano-based materials are used as carrier molecules to enhance the efficiency of anticancer drugs in targeted cancer therapy, such as polymeric micelles,<sup>3</sup> liposomes,<sup>4</sup> graphene oxide,<sup>5</sup> carbon quantum dots,<sup>6</sup> hollow carbon nanospheres,<sup>7</sup> carbon nanotubes,<sup>8</sup> and magnetic nanoparticles.<sup>9</sup> In recent decades, the potential role of mesoporous carbon nanoparticles as a carrier molecule has been widely used in biomedical applications.<sup>10</sup> A mesoporous carbon nanoparticle has unique properties such as good biocompatibility, water-solubility, high specific surface sides, a large porous structure that helps to enhance the loading capacity of anticancer drugs, and so forth. Mesoporous carbon nanoparticles have a high thermal capability, making them attractive in both photothermal and photodynamic therapy.<sup>11</sup> Zhang and co-workers synthesized the novel amide-dotted hollow carbon nanospheres loaded with siRNA (targeting multidrugresistance gene MDR1) and chemotherapeutics to achieve synergistic treatment to overcome

drug-resistant cancer. The synthesized nanospheres showed a higher loading percentage of both siRNA and chemotherapeutics, and it revealed the excellent performance of treating drug-resistant cancers both *in vitro* and *in vivo*.<sup>12</sup>

Doxorubicin is an effective class I anthracycline antibiotic, and it is considered an excellent broad-spectrum anticancer drug that induces cell apoptosis and treats several cancers.<sup>13</sup> Wang et al. developed a new HBS aptamer-functionalized DOX-loaded mesoporous carbon-silica composite, exhibiting higher cellular uptake in HER2 receptor-positive breast cancer cells (SK-BR-3) than normal breast epithelial cells (MCF-10A), and it has a potential chemo-photothermal effect against the targeted breast cancer therapy.<sup>14</sup> Chen et al. synthesized novel albumin-functionalized MoS<sub>2</sub> nanoparticles (MoS<sub>2</sub>@BSA) to load the doxorubicin drug, and it displayed better therapeutic cancer activity.<sup>15</sup> The loading percentage of doxorubicin plays an essential role in cancer treatment, and if it is low, it may reduce the effect of chemotherapy.

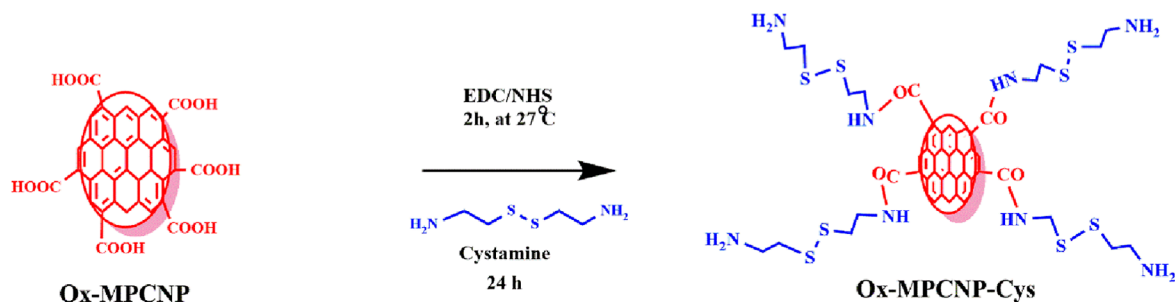
Received: September 1, 2021

Accepted: November 25, 2021

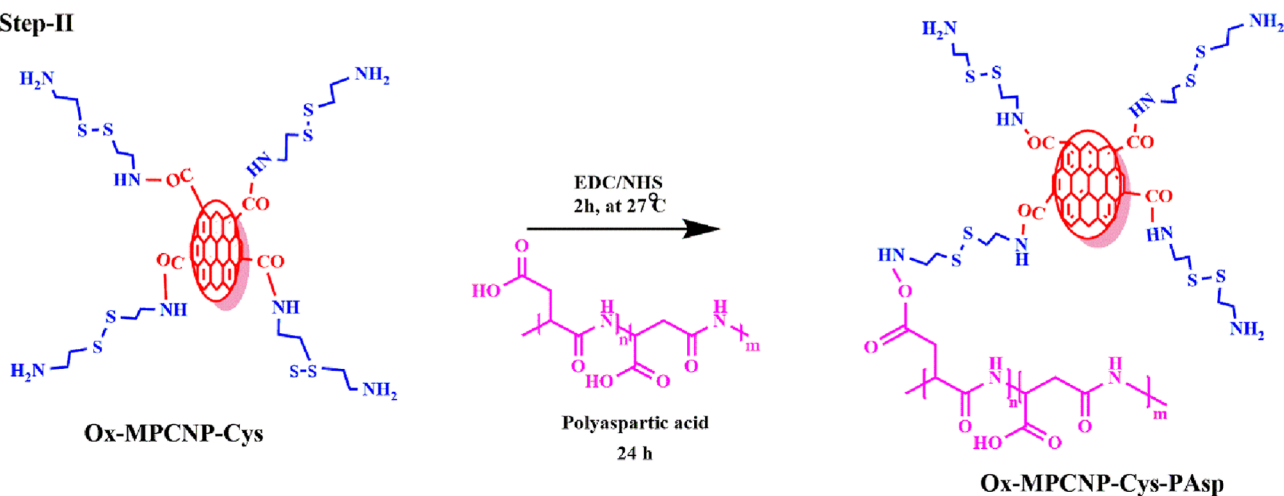
Published: December 10, 2021



## Step-I



## Step-II



## Step-III

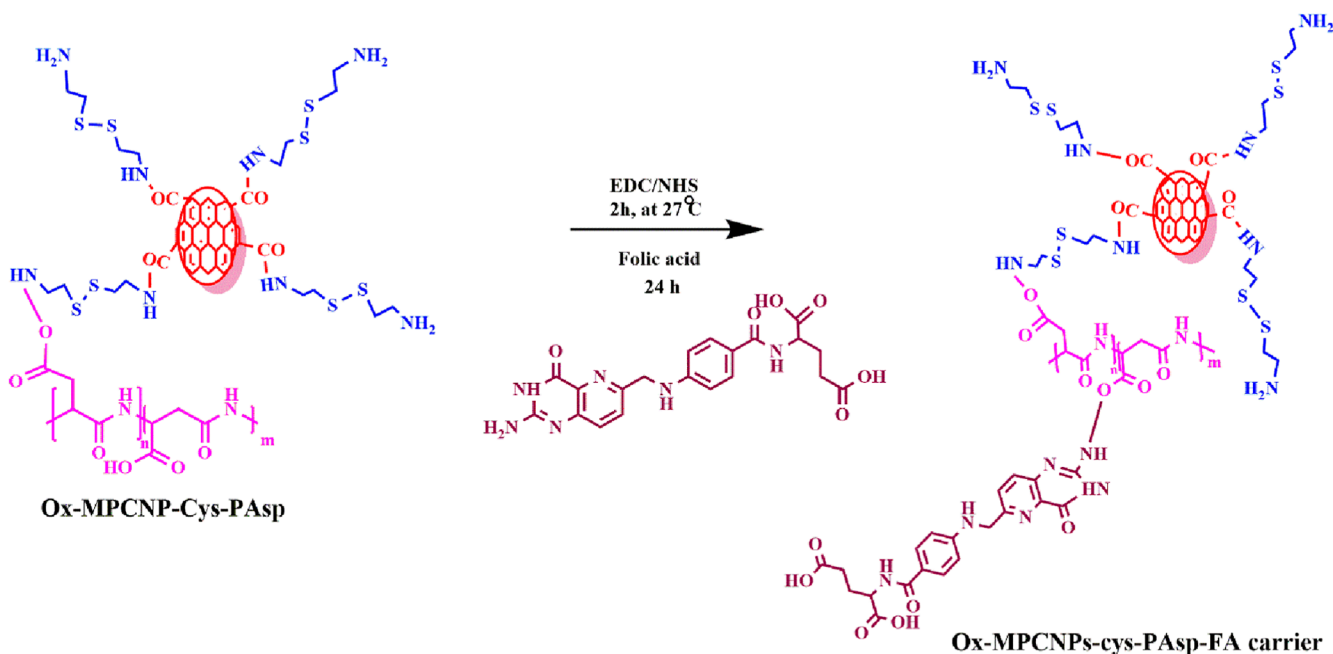


**Figure 1.** Overall schematic representation of the Ox-MPCNP-Cys-PAsp-FA nanocarrier.

Therefore, it is necessary to prepare a carrier with a high loading capacity or a drug with good biocompatibility so that drug-loading deficiency can be compensated to achieve successful cancer treatments.<sup>16</sup> Yang et al. synthesized metal-organic framework-derived carbon nanoparticles for imaging-guided photothermal/photodynamic therapy, and it significantly eliminated entire tumors with minimal side effects.<sup>17</sup>

The tumor-targeted drug delivery of anticancer drugs is one of the essential steps for cancer chemotherapy. Consequently, nowadays, a targeted drug delivery system effectively delivers the drugs into tumor sites.<sup>18</sup> For example, the pH-dependent release may enhance the permeability and retention effect (EPR) in solid tumors. The EPR effect can be achieved *via* different parameters such as leaking vasculature in the tumor, and the tumor vessel wall holes range from 200 nm to 2  $\mu$ m

with an average of 400 nm.<sup>19</sup> Moreover, most studies have suggested that nanoparticles with a 100–200 nm diameter can be easily accumulated in tumor cells.<sup>20–23</sup> Recently, receptor-mediated targeted drug delivery approaches have been developed to deliver the chemotherapeutic agents for tumor areas, using various targeting ligands such as folic acid (FA),<sup>24</sup> biotin,<sup>25</sup> peptides,<sup>26</sup> and genes.<sup>27</sup> Among them, cell-specific targeting ligands of FA (vitamin B9) were identified as an excellent targeting ligand that can avidly bind on folate receptors of over-expressed cancer cells such as breast, lung, ovarian, and cervical cancers.<sup>24</sup> Amino acids are the most active constituents in living organisms, helping to synthesize novel structural polymeric biomaterials with distinctive physicochemical, biological, biocompatibility, and biodegradability properties.<sup>28</sup> It can be successfully used for site-specific treatments with various smart internal and external responsive behaviors, including pH, temperature, redox, enzyme, light, and magnetic properties.<sup>29–31</sup> Among these, glutathione (GSH) triggered drug release. GSH acts as a reducing agent in the intracellular compartments to initiate the cleavage of a redox-sensitive disulfide bond in the nanocarrier and stimulates the burst drug release from the carrier. The concentration of GSH in the intracellular compartment is approximately  $\approx 2$ –10 mM.<sup>32</sup> The complexity of the GSH-rich cancer cell environment stimulates burst drug release from the redox-responsive nanocarriers.

Furthermore, pH-responsive drug release is one of the best ways to bring about intracellular controlled drug release. At the same time, cancer cells have a more acidic environment compared to normal tissue and bloodstream (pH=7.4), especially inside the endosomal (pH range 5.5–6.0) and lysosomal compartments (pH range 4.5–5.0). Wang et al. developed redox/enzyme dual-responsive disulfide-conjugated carbon dots with mesoporous silica nanoparticles using controlled targeted drug delivery and real-time bioimaging of cancer treatment. The synthesized material illustrates not only superior photostability but also good biocompatibility, which improve the targeting efficiency of A549 cell-overexpressed CD44 receptors.<sup>33</sup> Moreover, Wenhao Li et al. proposed that 5-FU-loaded polymer-coated graphitic carbon nanocages (GCNCs) exhibit a synergistic effect combined with photothermal therapy and chemotherapy to potentially inhibit tumor growth. The 5FU-GCNCs/CS improve the photothermal effect of GCNCs *in vivo* and the synergistic effect of photothermal therapy and chemotherapy, thus rushing the reduction of tumors. In addition, polymer-coated graphene-based materials exhibit good biosafety and high efficiency for cancer phototherapy.<sup>34</sup>

In this study, we designed a novel targeted and redox-responsive drug delivery system, “DOX/Ox-MPCNP-Cys-PAsp-FA”, in which an Ox-MPCNP-Cys-PAsp-FA nanocarrier was used as a carrier molecule to load chemotherapy anticancer drug doxorubicin on the Ox-MPCNP-Cys-PAsp-FA carrier through hydrogen bonding and  $\pi$ - $\pi$  interactions. The Ox/Ox-MPCNP-Cys-PAsp-FA carrier was characterized using different physicochemical studies. Also, the cytotoxicity, cell apoptosis, cell death, mitochondrial fragmentation, and nucleus damages of DOX/Ox-MPCNP-Cys-PAsp-FA were studied in MCF-7 breast cancer cells.

## 2. RESULTS AND DISCUSSION

### 2.1. Preparation of the Ox-MPCNP-Cys-PAsp-FA Nanocarrier.

In the present work, we have fabricated a mesoporous carbon nanosphere-based nanocarrier system

using breast cancer drug delivery. In brief, the Ox-MPCNP was loaded with DOX, followed by functionalization of Cys, PAsp, and FA. Initially, the Ox-MPCNP was synthesized through the hydrothermal process.<sup>35</sup> As illustrated in Figure 1, an Ox-MPCNP was attained *via* the oxidation of the MPCNP using H<sub>2</sub>O<sub>2</sub> by bath sonication. Then, the Ox-MPCNP was conjugated with Cys followed by EDC/NHS-mediated chemistry. After that PAsp was mixed with the solution as mentioned above and functionalized onto the surface of Ox-MPCNP-Cys through the EDC/NHS coupling reaction. Furthermore, the targeting ligand of FA was successfully conjugated with Ox-MPCNP-Cys-PAsp through the same amide bond reaction. Moreover, the anticancer drug DOX was loaded inside the Ox-MPCNP through the  $\pi$ - $\pi$  stacking and hydrogen-bonding interaction.

### 2.2. Chemical Structural Analysis.

Fourier transform infrared (FT-IR) spectroscopy was performed to confirm the structural elucidation of the Ox-MPCNP, Ox-MPCNP-Cys, Ox-MPCNP-Cys-PAsp, Ox-MPCNP-Cys-PAsp-FA, and DOX/Ox-MPCNP-Cys-PAsp-FA, and the results are given in Figure 2. The FT-IR spectrum in Figure 2a demonstrates that

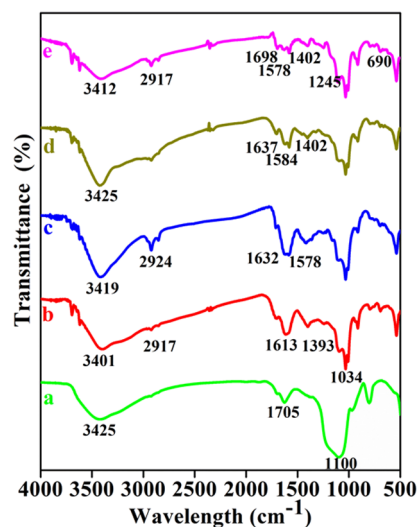


**Figure 2.** FT-IR spectra of the (a) Ox-MPCNP, (b) Ox-MPCNP-Cys, (c) Ox-MPCNP-Cys-PAsp, (d) Ox-MPCNP-Cys-PAsp-FA, and (e) DOX/Ox-MPCNP-Cys-PAsp-FA carrier.

Ox-MPCNP peaks that appeared at 3425, 1705, and 1100  $\text{cm}^{-1}$  are ascribed to  $-\text{OH}$ ,  $-\text{C}=\text{O}$ , and  $-\text{C}=\text{C}$  groups, respectively, which confirmed the presence of carboxylic groups on the MPCNP surface.<sup>39</sup> In that case, cystamine was conjugated to the carboxylic group of the Ox-MPCNP to obtain a new absorption peak at 1613 and 1393  $\text{cm}^{-1}$ , representing the amide-I stretching vibration, as given in Figure 2b.<sup>40</sup> In addition, the polymeric material of PAsp was grafted with cystamine to obtain another amide bond, as indicated in (Figure 2c); the peak was observed at 1578  $\text{cm}^{-1}$  (amide-II) which was assigned to the N–H bending vibration. Moreover, FA in PAsp to determine the new characteristic peak attributed to 1402  $\text{cm}^{-1}$  indicates the  $-\text{C}-\text{H}$  bending vibration of the amide-III bond through carboxylic groups of PAsp and the amino group of FA (Figure 2d). The Figure 2e spectrum represents DOX/Ox-MPCNP-Cys-PAsp-FA, and it manifests the Ox-MPCNP peaks of 1705  $\text{cm}^{-1}$  ( $-\text{C}=\text{O}$ ), and 1100  $\text{cm}^{-1}$  ( $\text{C}-\text{O}$ ) was shifted to lower regions such as 1698

$\text{cm}^{-1}$  ( $-\text{C}=\text{O}$ ) and  $1245\text{ cm}^{-1}$  ( $\text{C}-\text{O}$ ). This indicates that DOX was successfully bound through hydrogen bonding and  $\pi-\pi$  interactions<sup>41</sup> in the Ox-MPCNP-Cys-PAsp-FA nano-carrier. Furthermore, the newly appeared peak of  $690\text{ cm}^{-1}$  represents a plane of the  $-\text{N}-\text{H}$  stretching vibration of the DOX molecule, which also confirms the presence of DOX inside the core of the Ox-MPCNP-Cys-PAsp-FA carrier.<sup>42</sup>

**2.3. Crystalline Phase Analysis.** X-ray diffraction (XRD) analysis is an important tool for determining the crystalline-phase purity of as-synthesized materials, and the results are given in Figure 3. The XRD spectrum (Figure 3a) illustrates

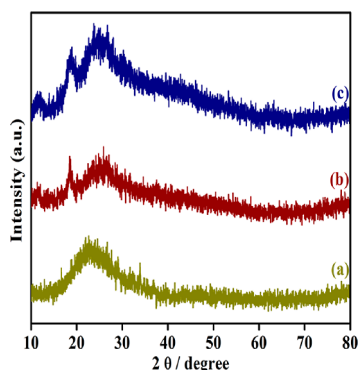


**Figure 3.** XRD Pattern of (a) Ox-MPCNP, (b) Ox-MPCNP-Cys-PAsp-FA, and (c) DOX/Ox-MPCNP-Cys-PAsp-FA carrier.

that only one prominent broad peak at around  $22\text{ \AA}$  (002 planes) corresponds to the amorphous nature of oxidized mesoporous carbon nanospheres.<sup>43</sup> Furthermore, the XRD pattern of the Ox-MPCNP-Cys-PAsp-FA carrier displays a similar pattern as that of the Ox-MPCNP but some newly occurred peaks at  $18\text{ \AA}$  and a decreased intensity, which suggests the formation of polymeric materials on the Ox-MPCNP surface, and it is given in Figure 3b. However, the DOX/Ox-MPCNP-Cys-PAsp-FA carrier clearly exhibits some predominant peaks at  $14$ ,  $23$ , and  $26\text{ \AA}$ , which reveals the semi-crystalline nature because DOX has physically interacted with the carrier (Figure 3c). Furthermore, the decreased crystalline nature could initiate the carrier's degradation and fast DOX release on tumor sites.<sup>44</sup>

**2.4. Morphological Analysis.** Scanning electron microscopy (SEM) and high-resolution transmission electron microscopy (HR-TEM) analyses were used to analyze the surface morphology of the as-synthesized Ox-MPCNP, Ox-MPCNP-Cys-PAsp-FA, and DOX/Ox-MPCNP-Cys-PAsp-FA carrier. Figure 4a indicates that a representative SEM image of the Ox-MPCNP shows a spherical-like structure.<sup>45</sup> Figure 4b also confirms the same spherical-like morphology of Ox-MPCNP-Cys-PAsp-FA. Furthermore, the SEM image of Figure 4c also provides the oval-shaped structure of the DOX/Ox-MPCNP-Cys-PAsp-FA carrier. From this Figure 4d–f, the HR-TEM images were also well-compared with SEM images of the Ox-MPCNP, Ox-MPCNP-Cys-PAsp-FA, and DOX/Ox-MPCNP-Cys-PAsp-FA carrier. The HR-TEM result demonstrates that the Ox-MPCNP represents the spherical-shape morphology (Figure 4d). Our results are well-correlated with those of Wang et al., who prepared the mesoporous carbon nanoparticles with a spherical-like morphology, as shown in Figure 4d.<sup>46</sup> In Figure 4e, the slightly enlarged and layered oval-shaped mesoporous carbon nanospheres were confirmed, which represents the anchoring

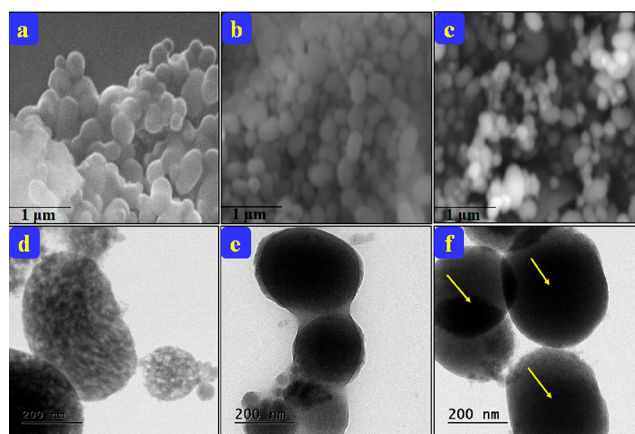


**Figure 4.** SEM images of (a) Ox-MPCNP, (b) Ox-MPCNP-Cys-PAsp-FA, and (c) DOX/Ox-MPCNP-Cys-PAsp-FA and HR-TEM images of (d) Ox-MPCNP, (e) Ox-MPCNP-Cys-PAsp-FA, and (f) DOX/Ox-MPCNP-Cys-PAsp-FA carrier.

of poly PAsp and FA on the surface of the Ox-MPCNP. The figure 4f image of the DOX/Ox-MPCNP-Cys-PAsp-FA carrier exhibits the dark intensity of the inner core, indicated by yellow arrow marks, representing the successful encapsulation of DOX on the Ox-MPCNP-Cys-PAsp-FA carrier, further to obtain the same oval-shaped morphology. Additionally, the small-size carriers enhance the pharmacokinetics and biodistribution of the drug and play an active role in *in vitro* and *in vivo* therapeutic applications.<sup>47</sup>

**2.5. Atomic Force Microscopy.** Atomic force microscopy (AFM) was used to investigate the surface topography, thickness, and height profile of the free and drug-loaded carriers, as displayed in Figure 5. The images of the free Ox-MPCNP-Cys-PAsp-FA carrier have an unshaped morphology, as shown in Figure 5a, whereas drug-loaded carriers exhibiting a sphere-like shape are seen in Figure 5d. The Ox-MPCNP-Cys-PAsp-FA carrier has an average thickness of  $446\text{ nm}$ , as represented in Figure 5b. After the encapsulation of DOX, the thickness of DOX/Ox-MPCNP-Cys-PAsp-FA is  $147\text{ nm}$  which (Figure 5e) indicates successful encapsulation of DOX onto the Ox-MPCNP. Moreover, the height profile of DOX/Ox-MPCNP-Cys-PAsp-FA is  $35.6\text{ nm}$  (Figure 5f), which is decreased compared to the free carrier height profile of  $288\text{ nm}$  (Figure 5c). Moreover, the results reveal that the drug was effectively encapsulated through  $\pi-\pi$  stacking and hydrogen-bonded with mesoporous carbon. Zhang et al. reported the attachment of physically interacted drug molecules on the graphitic structure, and our results are highly correlated with these approaches.<sup>48</sup>

**2.6. Surface Area and Pore Size Determination.** Building a targeted drug delivery nanocarrier system using mesoporous carbon nanospheres has the main advantages for cancer drug delivery. Several chemical functionalizations are necessary to bind the target molecules on the mesoporous carbon nanosphere surface. The Brunauer–Emmett–Teller (BET)  $\text{N}_2$  adsorption–desorption curves of the Ox-MPCNP, Ox-MPCNP-Cys, Ox-MPCNP-Cys-PAsp-FA, and DOX/Ox-MPCNP-Cys-PAsp-FA are given in Figure 6a–d. All the BET curves represent the type IV isotherm which is due to mesoporous materials.<sup>49</sup> The surface area of the Ox-MPCNP (Figure 6a) is high at  $261.23\text{ m}^2\text{ g}^{-1}$ . The total pore volume was calculated to be  $0.647\text{ cm}^3\text{ g}^{-1}$ , and the corresponding pore size was considered at  $8.33\text{ nm}$ . After functionalization of

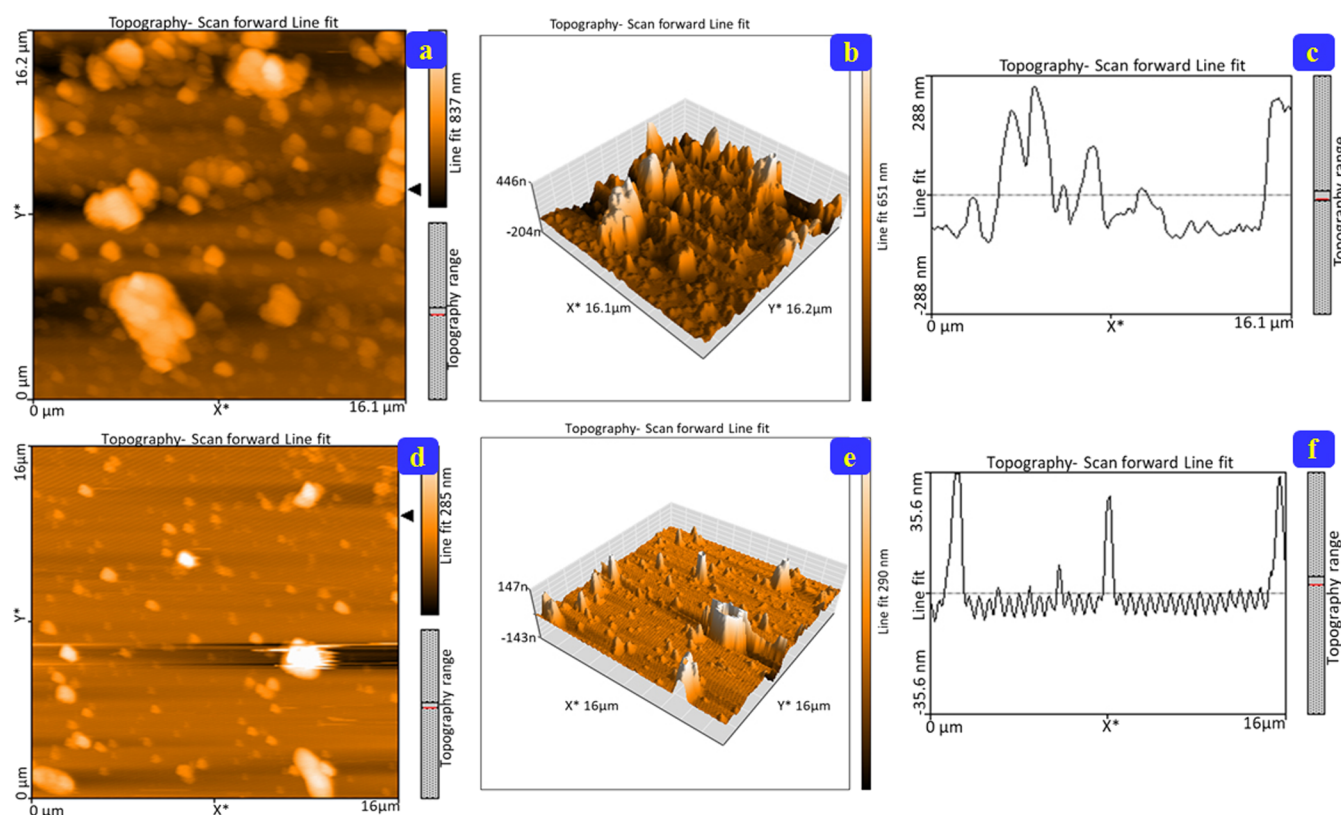


**Figure 5.** (a–c) 2D and 3D AFM images and the height profile of Ox-MPCNP-Cys-PAsp-FA and (d–f) 2D and 3D AFM images and the height profile of DOX/Ox-MPCNP-Cys-PAsp-FA.

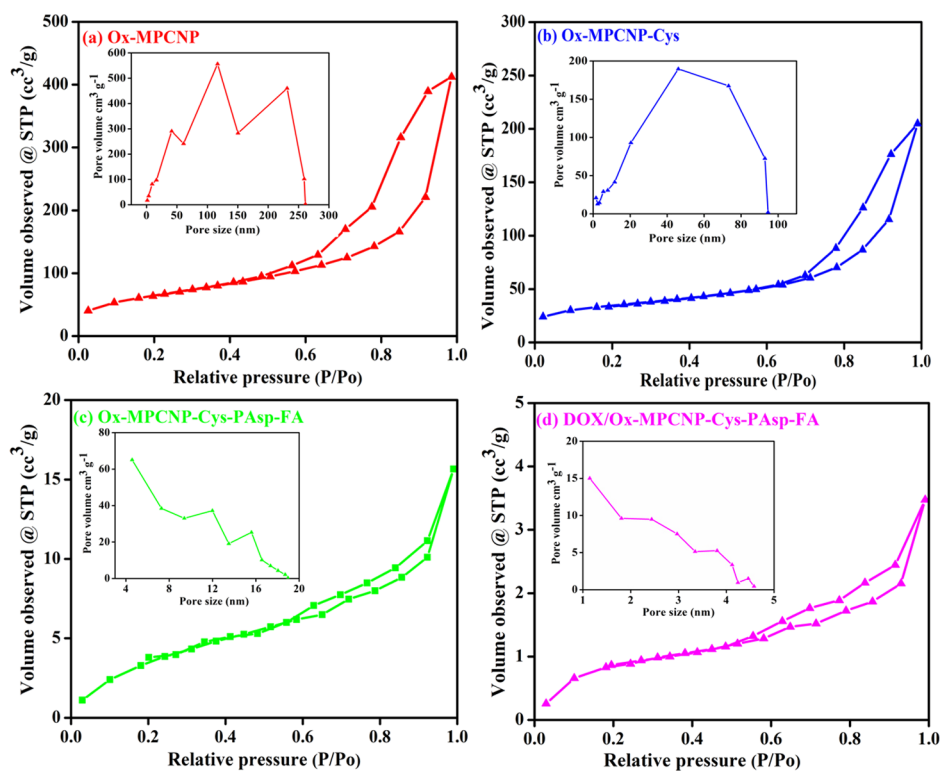


**Figure 6.** BET N<sub>2</sub> adsorption–desorption spectrum of (a) Ox-MPCNP, (b) Ox-MPCNP-Cys, (c) Ox-MPCNP-Cys-PAsp-FA, and (d) DOX/Ox-MPCNP-Cys-PAsp-FA. The inset images show the pore diameter of mesoporous materials.

cystamine, the surface area of Ox-MPCNP-Cys (Figure 6b) is decreased to 94.58 m<sup>2</sup> g<sup>-1</sup>, pore volume to 0.34 cm<sup>3</sup>/g<sup>-1</sup>, and

pore size to 6.46 nm, which determines the successful conjugation of cystamine to the Ox-MPCNP surface. In

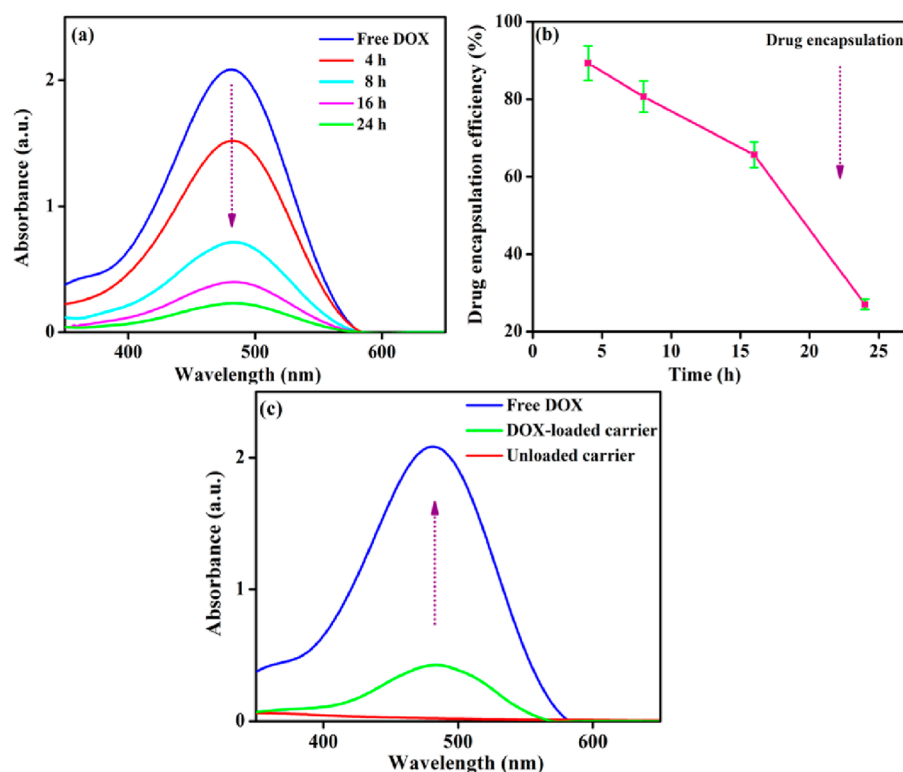


**Figure 7.** (a) Drug EE, (b) bar diagram of drug EE, and (c) drug-loading capacity of DOX in Ox-MPCNP-Cys-PAsp-FA.

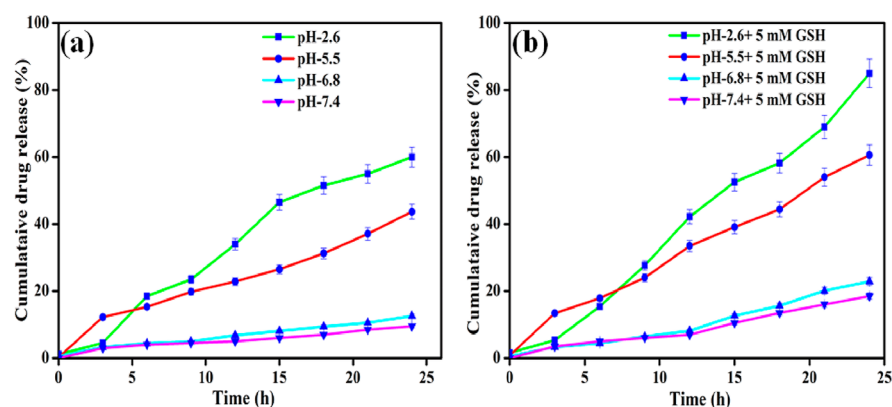


**Figure 8.** Cumulative drug-release profiles under different conditions. (a) pH (2.6, 5.5, 6.8, and 7.4) and (b) 5 mM GSH concentrations of the DOX of the Ox-MPCNP-Cys-PAsp-FA carrier.

addition, Ox-MPCNP-Cys was covered with PAsp and the targeting ligand, and the surface areas of Ox-MPCNP-Cys-PAsp-FA (Figure 6c) were significantly reduced to  $18.96 \text{ m}^2 \text{ g}^{-1}$ , and the pore volume is  $0.028 \text{ cm}^3 \text{ g}^{-1}$ , and pore size is  $2.29 \text{ nm}$ . Furthermore, DOX was encapsulated on inner mesoporous core sites, which demonstrates the blockage of the mesoporous core entirely due to the DOX molecule, and the surface area of the DOX/Ox-MPCNP-Cys-PAsp-FA carrier (Figure 6d) was  $4.58 \text{ m}^2 \text{ g}^{-1}$ , and pore volume was  $0.005 \text{ cm}^3 \text{ g}^{-1}$ , and pore size was  $2.24 \text{ nm}$ . Moreover, the mesoporous properties of carbon materials could provide an applicable cavity for loading and releasing properties in cancer drug delivery systems.<sup>50</sup>

**2.7. UV-Vis Analysis.** The encapsulation and loading capacity were determined to confirm the high amount of DOX on the Ox-MPCNP-Cys-PAsp-FA carrier. The encapsulation efficiency (EE) of DOX, as shown in Figure 7, is 89.37%

because it corresponds to the surface area at  $18.96 \text{ m}^2 \text{ g}^{-1}$  and porous volume at  $0.028 \text{ cm}^3 \text{ g}^{-1}$  and pore size at  $2.29 \text{ nm}$  of the Ox-MPCNP-Cys-PAsp-FA nanocarrier cavity size in BET analysis. The loading capacity of DOX was analyzed using UV-visible spectroscopy, and 16.40% of DOX was achieved. The higher EE percentage of DOX is confirmed, and the results are given in Figure 7a,b, and the loading capacity of DOX is given in Figure 7c. The EE of DOX was highly attained on mesoporous carbon with different time intervals through hydrogen bonding and  $\pi$ - $\pi$  stacking interactions of DOX with the surface basal plane of carbon layers.<sup>51</sup>

**2.8. In Vitro Drug-Release Measurements.** The pH and GSH redox-responsive drug-release behavior of the DOX/Ox-MPCNP-Cys-PAsp-FA carrier was measured under different conditions (pH 2.6, 5.5, 6.8, and 7.4) with and without the presence of the 5 mM GSH concentration. The cumulative drug-release rate of the DOX-loaded Ox-MPCNP-Cys-PAsp-

FA carrier is given in Figure 8a,b. The redox-responsive cleavage of the disulfide bond will cause the burst release of DOX from Ox-MPCNP species on the polymeric backbone of the amino acid in cancer-affected areas.<sup>52</sup> As shown in Figure S1a,e, at pH 2.6, the 5 mM GSH-containing drug-loaded nanocarrier exhibits a relatively high drug-release behavior at 84.34% and without GSH conditions shows 60.41% release, which was observed in 24 h. It may be due to the reduction of a disulfide bond in cystamine in the Ox-MPCNP system. However, a maximum amount of drug release was observed at pH 5.5  $\approx$  60.6 (with GSH) and  $\approx$ 43.7% (without GSH), as shown in Figure S1b,f. The DOX release of pH 6.8 and 7.4 is much lower compared to that of pH 2.6 and pH 5.5, and the release percentage of pH 6.8 is 44.9% (with GSH) and 14.6% (without GSH), and the release percentage of pH 7.4 is 10% (without GSH), and the release percentage of pH 7.4 is 18.5% (with GSH). In addition, the GSH-responsive drug release property of pH 2.6 is significantly higher than that of pH 5.5, 6.8, and 7.4 (Figure S1). Overall, the DOX/Ox-MPCNP-Cys-PAsp-FA carrier shows admirable pH- and GSH-responsive behaviors and therefore the hydrogen bonding and  $\pi$ - $\pi$  stacking interaction between the DOX and Ox-MPCNP-Cys-PAsp-FA carrier system. On the other hand, DOX is a hydrophilic and highly stable acidic medium, which caused the easy protonation of amine groups in the DOX molecule,<sup>53,54</sup> so the DOX was quickly released in acidic environments compared to other pH conditions at 5.5, 6.8, and 7.4. The -pH- and -GSH-responsive nanocarrier had great potential and outstanding property in biomedical applications.<sup>55</sup>

**2.9. In Vitro Biodegradation Analysis.** The *in vitro* biodegradable and morphological changes of the DOX/Ox-MPCNP-Cys-PAsp-FA carrier were studied using different pH conditions (pH—2.6, 5.5, and 6.8) with a 5 mM concentration of GSH at room temperature, and the results are given in Figure 9. As shown in Figure 9a–c, SEM images of a pH-dependent biodegrading nature were identified. The acidic pH 2.6 environment introduces the DOX/Ox-MPCNP-Cys-PAsp-FA carrier morphology that was entirely changed and creates swelled large particles which indicates the fast-biodegrading

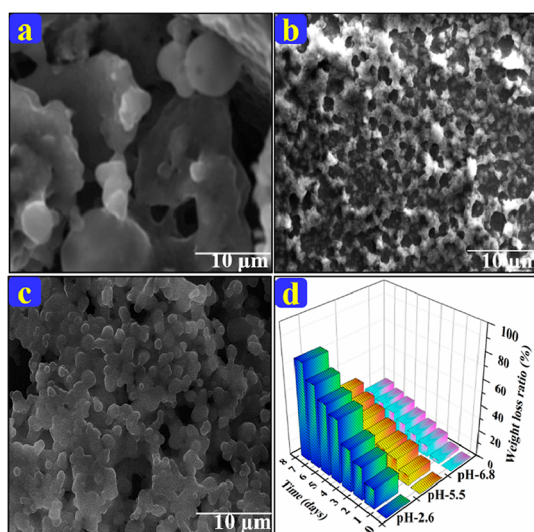


**Figure 9.** DOX/Ox-MPCNP-Cys-PAsp-FA carrier bio-degradation SEM images under various pH conditions (a) 2.6, (b) 5.5, and (c) 6.8 with a 5 mM GSH concentration level and (d) degradation study of the DOX/Ox-MPCNP-Cys-PAsp-FA carrier in a bar diagram.

disulfide and amide bonds incorporated into the DOX/Ox-MPCNP-Cys-PAsp-FA carrier carbon skeleton, and maximum weight loss was observed at 75.4% after the 7 day incubation period. In Figure 9b, pH 5.5 manifests slight morphology changes that were identified, and the weight loss amount is 38.5%. Although in Figure 9c,, no complete morphology changes were observed after seven days of biodegradation, the weight loss amount is 25.3% at pH 6.8. These results demonstrate that the hybridized disulfide and amide bonds provided the Ox-MPCNP with enhanced biodegradation capability to reduce the microenvironment compartment.<sup>56</sup> The time-dependent degradation rate of the DOX/Ox-MPCNP-Cys-PAsp-FA carrier is given in Figure 9d.

**2.10. In Vitro Cell Toxicity (Lactate Dehydrogenase Assay).** Lactate dehydrogenase (LDH) is a stable cytosolic enzyme that is released upon cell lysis, and it is used to detect the *in vitro* cell toxicity and cell deaths of breast cancer cells.<sup>57</sup> The cell-membrane damages of MCF-7 after treatment with different concentrations (1.25, 2.5, 5, 10, 20, 40, and 80  $\mu$ g/mL) of Ox-MPCNP, Ox-MPCNP-Cys-PAsp-FA, and DOX/Ox-MPCNP-Cys-PAsp-FA carriers are measured by the release of LDH using CytoTox96 assay, and the results are given in Figure 10. The treated free DOX concentrations (0.1, 0.25, 0.5,

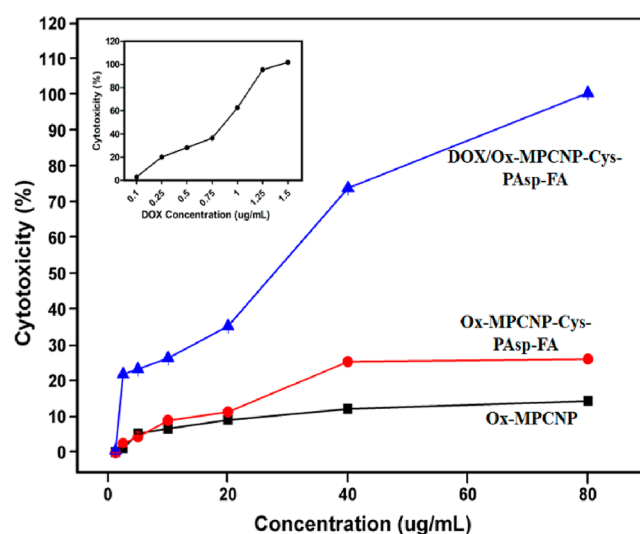


**Figure 10.** Cell toxicity of MCF-7 cell lines after being treated with different concentrations of the DOX (0.1–1.25  $\mu$ g/mL), Ox-MPCNP, Ox-MPCNP-Cys-PAsp-FA, and DOX/Ox-MPCNP-Cys-PAsp-FA after 24 h, measured using LDH assay.

0.75, 1, 1.25, and 1.5  $\mu$ g/mL) were measured using CytoTox96 assay, and the results are given in Figure 10 (inset). The percentage of toxicity gradually increased the concentration of as-prepared nanomaterials. As shown in Figure 10, fewer cell toxicity effects were found in Ox-MPCNP- and Ox-MPCNP-Cys-PAsp-FA-treated cancer cells. The cell viability was still more than 80% after incubation with the Ox-MPCNP and Ox-MPCNP-Cys-PAsp-FA for 24 h up to a concentration of 80  $\mu$ g/mL. The cell toxicity effect exhibits that DOX/Ox-MPCNP-Cys-PAsp-FA had a significantly higher toxicity effect than the Ox-MPCNP and Ox-MPCNP-Cys-PAsp-FA. As seen in Figure 10 (inset), free DOX makes acute cell damage to the measured extracellular release of LDH and reduces cell viability in MCF-7 cells. The  $IC_{50}$  values of free DOX and DOX/Ox-MPCNP-Cys-PAsp-FA in MCF-7 cells were 0.89 and 27.7  $\mu$ g/

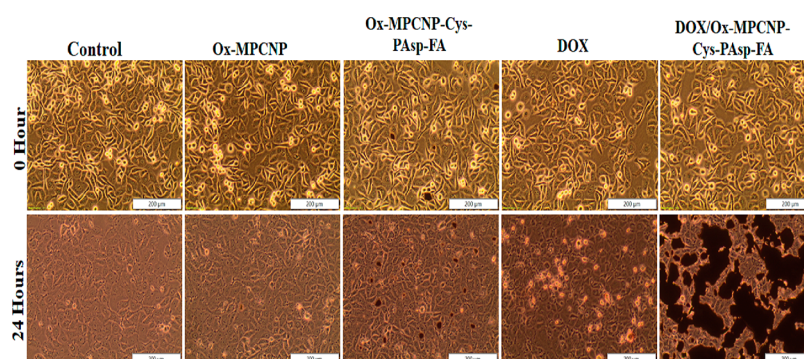


**Figure 11.** *In vitro* morphological changes of the MCF-7 cell line after treatment with the control, Ox-MPCNP, Ox-MPCNP-Cys-PAsp-FA, DOX, and DOX/Ox-MPCNP-Cys-PAsp-FA carrier for 24 h period observed using inverted light microscopy.

mL respectively, indicating disruption of the cell-membrane damages. The higher cell toxicity effect of DOX/Ox-MPCNP-Cys-PAsp-FA may be attributed to receptor-mediated endocytosis by MCF-7 cells,<sup>58</sup> which increases the drug concentration in the intracellular environment.

**2.11. *In Vitro* Morphological Analysis.** *In vitro* morphological changes of MCF-7 cells were observed by inverted light microscopy, and the results are given in Figure 11. There was an extreme morphology change in the MCF-7 cells after 24 h treatment. The Ox-MPCNP-, Ox-MPCNP-Cys-PAsp-FA-, DOX-, and DOX/Ox-MPCNP-Cys-PAsp-FA-treated MCF-7 display intrinsic cell damage and cell shrinkages compared with the control group. The use of DOX/Ox-MPCNP-Cys-PAsp-FA caused more significant cell destruction compared to the action of free DOX itself, while in the Ox-MPCNP, the Ox-MPCNP-Cys-PAsp-FA-treated cell line shows smaller morphology changes than that treated with free DOX alone.

**2.12. Annexin V/PI Staining.** Cell apoptosis of the control, Ox-MPCNP, Ox-MPCNP-Cys-PAsp-FA, DOX, and DOX/Ox-MPCNP-Cys-PAsp-FA carrier on MCF-7 cells was measured using annexin V-FITC and PI by flow cytometry, and the results are given in Figure 12a. The quantitative cell apoptotic cell death on the MCF-7 cell line is shown in Figure 12b. In Figure 12a, the MCF-7 cells were treated with the appropriate concentration of as-prepared materials. The percentage of cell apoptosis induced by free DOX and each material was evaluated after 24 h of incubation. In apoptotic cells, the membrane phospholipid phosphatidylserine (PS) is exposed to the external cellular environment due to translocation from the inner to the outer surface of the plasma membrane.<sup>59</sup> Annexin V could serve as a sensitive probe for cell apoptosis analysis. The flow cytometry results of the MCF-7 cells (Figure 12a) exhibit the early apoptosis percentage of the control (36%), Ox-MPCNP (38.5%), Ox-MPCNP-Cys-PAsp-FA (43.2%), free DOX (52.6%), and DOX/Ox-MPCNP-Cys-PAsp-FA (58%) and the late apoptosis percentage of the control (2.1%), Ox-MPCNP (1.7%), Ox-MPCNP-Cys-PAsp-FA (1.3%), free DOX (1.2%), and DOX/Ox-MPCNP-Cys-PAsp-FA (36.8%). Moreover, the annexin V/PI flow cytometry confirmed that DOX was effectively delivered on MCF-7 cells by DOX/Ox-MPCNP-Cys-PAsp-FA. It was confirmed that the release of DOX from the nanocarrier shows apoptotic cell death.

**2.13. Nucleus Staining Analysis.** Mitochondria play an essential role in controlling cell growth and death.<sup>60</sup> An as-prepared material was treated with MCF-7 cells and

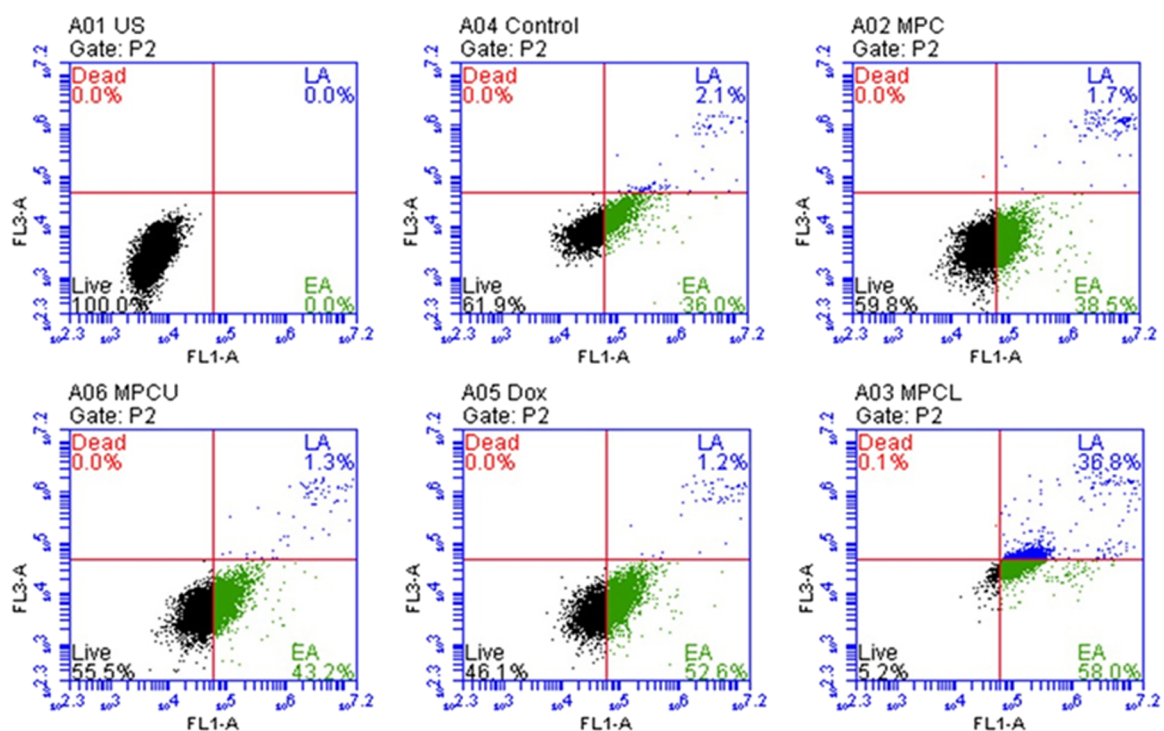
investigated for the mitochondria fragmentation and cellular nucleus damage stained with Mito Tracker (green) and DAPI (blue) by fluorescence microscopy, and the results are given in Figure 13. It exhibits that nearly no green fluorescent signals overlapped with the blue fluorescent of the nucleus in MCF-7 cells treated for 24 h with the control, Ox-MPCNP, Ox-MPCNP-Cys-PAsp-FA, and DOX. However, the green fluorescent signal mostly overlapped with the blue fluorescent of the nucleus in MCF-7 cells treated with DOX/Ox-MPCNP-Cys-PAsp-FA. It indicates that the targeting moiety of FA could guide the delivery of DOX into the cell nucleus and initiate cell death. Furthermore, the DOX/Ox-MPCNP-Cys-PAsp-FA would possibly inhibit the cell proliferation of MCF-7 cells and exhibit mitochondria fragmentation and cellular nucleus damages and shrinkages. Overall, DOX/Ox-MPCNP-Cys-PAsp-FA could have a high inhibition effect of DOX against both mitochondria and nucleus.

### 3. CONCLUSIONS

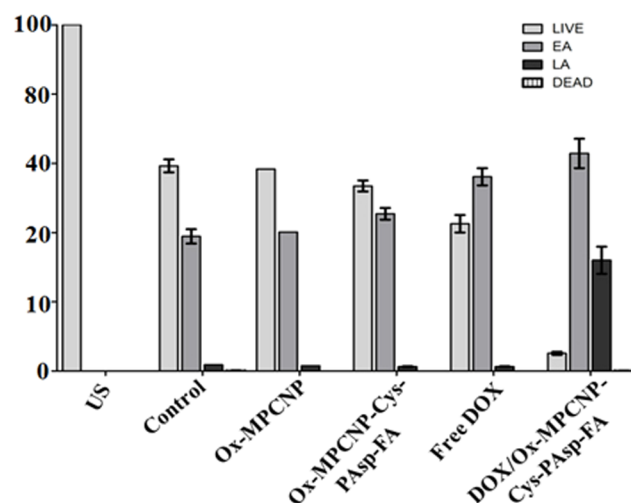
In summary, we successfully designed a novel targeted and redox-responsive drug delivery system doxorubicin-loaded mesoporous carbon nanospheres based on a FA-functionalized nanocarrier “DOX/Ox-MPCNP-Cys-PAsp-FA” for breast cancer therapy. The as-prepared nanocarrier had a suitable EE of DOX (89.37%), loading capacity (16.40%), and uniform porous sphere shapes. The developed DOX/Ox-MPCNP-Cys-PAsp-FA carrier molecule demonstrated the smart and quick drug-release behavior in response to thiol-reducing agents such as GSH and pH in simulated cancerous tissue medium. The enhanced cytotoxic effect of DOX/Ox-MPCNP-Cys-PAsp-FA was observed against MCF-7 cancer cells. The fluorescence microscopy and flow cytometry results confirmed that the DOX/Ox-MPCNP-Cys-PAsp-FA carrier remarkably enhanced cellular drug uptake *via* endocytosis and induced cancer cell apoptosis *in vitro*. The results demonstrate DOX/Ox-MPCNP-Cys-PAsp-FA-targeted receptor-mediated breast cancer cells, leading to improved anticancer activity by FR-mediated endocytosis. Overall, the DOX/Ox-MPCNP-Cys-PAsp-FA nanocarriers with superior physio-chemical, controllable, and pH- and GSH-dependent drug-releasing profiles have been successfully reported in this work. Overall, the results showed that the synthesized DOX/Ox-MPCNP-Cys-PAsp-FA nanocarriers could be a more promising material for drug delivery in anti-tumour applications.

(A)

## APOPTOSIS ASSAY USING ANNEXIN AND PI – FLOW CYTOMETRY



(B)



	Live		EA		LA		Dead	
	Avg	SD	Avg	SD	Avg	SD	Avg	SD
US	100	0	0	0	0	0	0	0
Control	59.26667	1.897952	38.9	2.070427	1.8	0	0.066667	0.094281
MPC	58.33333	0	40.13333	0	1.533333	0	0	0
MPCU	53.43333	1.600694	45.4	1.687207	1.266667	0.124722	0	0
DOX	42.53333	2.522345	56.1	2.477902	1.3	0.08165	0	0
MPCL	5.1	0.454606	62.86667	4.224005	32	3.919184	0.066667	0.04714

**Figure 12.** (a) Flow cytometry analysis of apoptosis in MCF-7 treated with the Ox-MPCNP, Ox-MPCNP-Cys-PAsp-FA, DOX, and DOX/Ox-MPCNP-Cys-PAsp-FA carrier for 24 h; (b) quantitative cell apoptosis analysis of MCF-7 cells after treatment with the Ox-MPCNP, Ox-MPCNP-Cys-PAsp-FA, DOX, and DOX/Ox-MPCNP-Cys-PAsp-FA carrier for 24 h using flow cytometry.

## 4. EXPERIMENTAL SECTION

**4.1. Materials.** Hexadecyltrimethylammonium bromide (CTAB), resorcinol, formaldehyde, tetraethyl orthosilicate (TEOS), ammonia (NH<sub>3</sub>), cystamine (Cys), hydrogen

fluoride (HF), and poly aspartic acid (PAsp) were obtained from HiMedia Pvt Ltd., India. Doxorubicin (DOX), FA, 1-ethyl-3-(3-dimethylamoniopropyl) carbodiimide (EDC-HCl), *N*-hydroxysuccinimide (NHS), ethanol, and acetone were

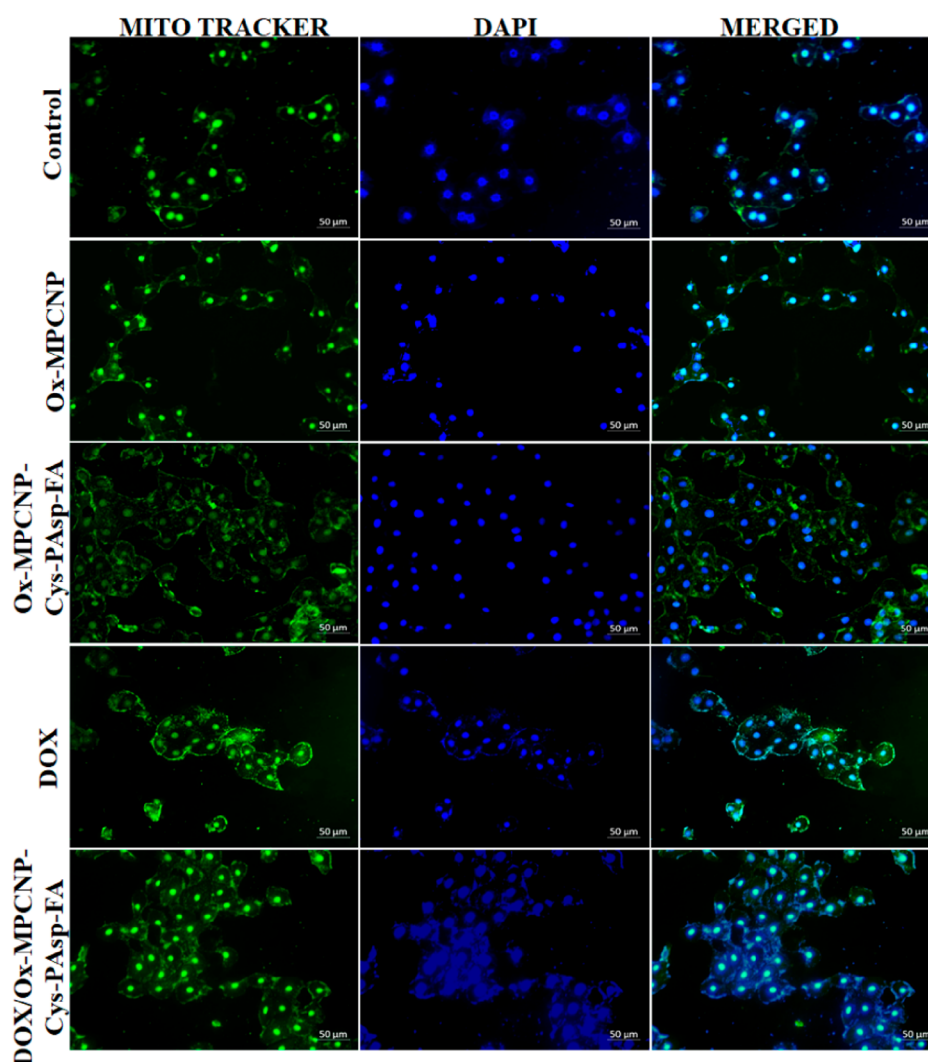


**Figure 13.** Assessment of the nuclear morphology in MCF-7 cells stained with Mito Tracker and DAPI. The images were taken with a fluorescence microscope.

purchased from Sigma-Aldrich, Mumbai, India. All other chemicals and reagents used in the study were of analytical grade. Double distilled water was used for all the experiments.

**4.2. Synthesis of Oxidized Mesoporous Carbon Nanospheres (Ox-MPCNPs).** Briefly, 1.2 g of CTAB and 0.4 g of resorcinol were dissolved in a 60 mL mixture solution containing 50 mL of water and 10 mL of ethanol solution. The solution was systematically and magnetically stirred at 400 rpm under room temperature.<sup>35</sup> Subsequently, 0.5 mL of ammonia ( $\text{NH}_3$ ) solution was slowly added to the solution, and the magnetic stirrer process was continued for another 20 min. Afterward, 0.6 mL of formaldehyde solution was injected and mixed, and the solution was permitted to stand for 2 min. In addition to this TEOS was added suddenly to the above-mentioned reaction with stirring for 24 h at room temperature (27 °C). At that time, the solution was usually cooled and transferred into a Teflon-lined autoclave at 80 °C for a 24 h hydrothermal process. The obtained brownish solid product was centrifuged at 5000 rpm for 30 min and washed with double distilled water, and then, the obtained compound was calcined at 700 °C for 3 h at a rate of 1 °C/min under a  $\text{N}_2$  atm to obtain the mesoporous carbon/silica nanospheres. Then, the hard silica template was removed by immersion in

15% HF aqueous solution for 24 h followed by washing with double distilled water. Typically, 100 mg of MPCNPs (mesoporous carbon nanospheres) was dispersed in 50 mL of  $\text{H}_2\text{O}_2$  solution and bath-sonicated for 4 h. After this, it was centrifuged, washed, and dried in a hot air oven (60 °C) for 24 h. Finally, oxidized mesoporous carbon nanospheres (Ox-MPCNPs) were obtained.

**4.3. Synthesis of Cystamine-Functionalized Oxidized Mesoporous Carbon Nanospheres (Ox-MPCNP-Cys).** 500 mg of mesoporous carbon nanoparticles was dispersed in 50 mL of distilled water, and to this, separately dissolved 20 mL of distilled water containing 100 mg of EDC-HCl and 100 mg of NHS solutions was simultaneously added and magnetically stirred for 2 h.<sup>36</sup> After this, the stirred carboxyl group Ox-MPCNP was activated and 10 mL of 1 g cystamine-dihydrochloride (DAPI) solution was added to it and was further continuously magnetically stirred for another 24 h at 27 °C. Finally, the obtained product was washed with double distilled water and dried in a hot air oven (60 °C) for 6 h.

**4.4. Synthesis of Poly Aspartic Acid-Functionalized Oxidized Mesoporous Carbon Nanospheres (Ox-MPCNP-Cys-PAsp).** A carboxylic group of poly aspartic acid was activated using a EDC.HCL/NHS-mediated coupling

reaction. Initially, 500 mg of poly aspartic acid was dissolved in 50 mL of distilled water and 100 mg of EDC-HCL and 100 mg of NHS were added to the solution and magnetically stirred for 2 h at 27 °C. Then, 250 mg of Ox-MPCNP-Cys was dispersed in 20 mL of double distilled water and this solution was added slowly to the above-mentioned reaction mixture for 24 h with magnetic stirring at 27 °C.

**4.5. FA-Functionalized Ox-MPCNP-Cys-PAsp (Ox-MPCNP-Cys-PAsp-FA).** The modification of Ox-MPCNP-Cys-PAsp with FA to form the Ox-MPCNP-Cys-PAsp-FA nanocarrier was performed by an EDC/NHS-mediated reaction.<sup>37</sup> Typically, 250 mg of Ox-MPCNP-Cys-PAsp was dispersed in 20 mL of double distilled water and mixed with 100 mg of EDC-HCl and 100 mg of NHS under vigorous magnetic stirring for 2 h. Then, a 5 mL DMSO solution containing (100) mg of FA solution was added to it. The reaction was continued for 12 h under dark reaction conditions. After the reaction was completed, the obtained product was washed with distilled water and further dried in a hot air oven at 50 °C for 6 h.

**4.6. Synthesis of Doxorubicin-Loaded Cystamine-Functionalized Oxidized Mesoporous Carbon Nanospheres (DOX/Ox-MPCNP-Cys-PAsp-FA).** The drug-loading procedure was carried out using the solvent evaporation method.<sup>38</sup> 25 mg of Ox-MPCNP-Cys-PAsp-FA was dispersed in 10 mL of distilled water, and the anticancer drug doxorubicin (2.5 mg) was dissolved in a 10 mL ethanol solution that was added dropwise. In addition, the mixture was ultrasonicated for (15 min), and the content was magnetically stirred overnight under dark reaction conditions at 27 °C. Then, the solution was centrifuged and washed with distilled water and further dried in a hot air oven at 60 °C for 12 h.

**4.7. Characterization Studies.** **4.7.1. FT-IR Spectroscopy Analysis.** The synthesized Ox-MPCNP, Ox-MPCNP-Cys, Ox-MPCNP-Cys-PAsp, Ox-MPCNP-Cys-PAsp-FA, and DOX/Ox-MPCNP-Cys-PAsp-FA were mixed with KBr powder and compressed to form a pellet. As-prepared KBr pellets were scanned in the spectral (FT-IR, Spectrum GX-1, Perkin Elmer, USA) region of 4000–400 cm<sup>-1</sup>.

**4.7.2. XRD Analysis.** The crystalline-phase properties of as-prepared materials were analyzed using a Philips 1710 X-ray powder diffractometer (Philips Electronic Instruments, Inc., Mahwah, NJ) with a copper target (Cu K $\alpha$ 1,  $\lambda$  = 1.54056 Å) and a nickel filter at a voltage of 40 kV and a current of mA.

**4.7.3. Morphological Analysis (SEM and HR-TEM).** The surface morphology of synthesized materials was characterized by scanning electron microscopy (VEGA3SB, TESCAN, and Czech). The samples were put on a carbon tape, and the less-conducting samples were to be gold-sputtered before taking them onto the specimen stage of SEM. The coating was achieved at 25 mA for at least 60 s. The scanning range was performed under high vacuum and at ambient room temperature with a 20–30 kV beam voltage. Moreover, in the HR-TEM study, a few droplets of as-prepared samples were placed on a carbon grid. The grids were tested under a HR-TEM TECNAI F30 at a voltage of 80 kV.

**4.7.4. Atomic Force Microscopy.** Surface roughness, height profile, and topography of the as-fabricated materials were characterized using AFM analysis. Images were recorded using a BT 02218 Nanosurf, Liestal, Switzerland.

**4.7.5. BET Analysis.** The specific surfaces area and pore size distribution of the Ox-MPCNP, Ox-MPCNP-Cys, Ox-MPCNP-Cys-PAsp-FA, and DOX/Ox-MPCNP-Cys-PAsp-FA were

analyzed using a BET and Barret–Joyner–Halenda model, respectively.

**4.7.6. Drug EE and Loading-Capacity Analysis.** Doxorubicin-containing ethanol solution was slowly added to Ox-MPCNP-Cys-PAsp-FA solutions at 150 rpm for magnetic stirring at room temperature. The EE was measured by UV–vis spectroscopy (Shimadzu-UV-1800, Japan) at different time intervals and calculated using eq 1. Furthermore, the loading capacity (LC) of Ox-MPCNP-Cys-PAsp-FA and the DOX absorption intensity were measured by UV–vis spectroscopy at 484 nm and calculated using eq 2.

$$EE (\%) = \frac{\text{the total amount of drug} - \text{free amount of drug}}{\text{the total amount of drug}} \times 100 \quad (1)$$

$$LC (\%) = \frac{\text{the total amount of drug} - \text{free amount of drug}}{\text{weight of the dried nanocarrier}} \times 100 \quad (2)$$

**4.7.7. In Vitro Drug-Release Studies.** The *in vitro* drug-release profiles of DOX from the nanocarriers were studied using various pH environments (2.6, 5.5, 6.8, and 7.4) with and without the 5 mM GSH concentration. We studied the pH- and GSH-responsive drug-release properties of the DOX/Ox-MPCNP-Cys-PAsp-FA carrier at 37 °C. Typically, 100 mg of the nanocarrier was dispersed in 2 mL of PBS solution, transferred to the dialysis membrane bag (molecular weight cut-off 14,000 Da), and placed into 250 mL of release medium under magnetic stirring at 37 °C. At predetermined time intervals, 2 mL of release medium was collected to analyze released doxorubicin. Then, an equal volume of fresh PBS solution was added to maintain the sink conditions. The released DOX was determined spectrophotometrically at 484 nm.

**4.7.8. Biodegradation and Weight Loss Studies.** *In vitro* biodegradation and weight-loss behavior of the DOX/Ox-MPCNP-Cys-PAsp-FA carrier were studied under different pH conditions (2.6, 5.5, and 6.8) with a 5 mM concentration of GSH. Briefly, 100 mg of the drug-loaded carrier was immersed in a 10 mL pH solution, and GSH was slowly added to it. Then, the samples were incubated with GSH-responsive activity at 37 °C with constant magnetic stirring at 100 rpm. The DOX/Ox-MPCNP-Cys-PAsp-FA carrier system was collected, centrifuged, and washed with distilled water at predetermined time intervals. After that the DOX/Ox-MPCNP-Cys-PAsp-FA carrier was dried using a lyophilizer (Sub Zero lyophilizer, Chennai, India). The weight loss of the DOX/Ox-MPCNP-Cys-PAsp-FA carrier was determined using eq 3.

$$\text{Degradation} (\%) = \frac{W_0 - W_t}{W_0} \times 100 \quad (3)$$

$W_0$ —weight of the initial carrier,  $W_t$ —weight of the dried carrier.

**4.8. Biological Studies.** **4.8.1. Cell Culture.** The human breast cancer cell line (MCF-7; ATCC HTB-22) was obtained from ATCC. The cell culture growth medium was Dulbecco's modified Eagle's medium (DMEM; D5796) obtained from Sigma-Aldrich. The cells were maintained in DMEM supplemented with 10% fetal bovine serum (FBS, 10499–044; Gibco), 1% penicillin–streptomycin (P4333), and 1% amphotericin B (A2943) in 85% humidified atmosphere at 37

°C and 5% CO<sub>2</sub>. CytoTox 96 non-radioactive cell toxicity assay was obtained from Promega Corporation (Madison, WI, USA). We bought the FITC Annexin V Apoptosis detection kit from BD Pharmingen (San Jose, CA, USA) for flow cytometry.

**4.8.2. Cell Toxicity (LDH Assay).** The cell-toxicity effect of DOX, Ox-MPCNP, Ox-MPCNP-Cys-PAsp-FA, and DOX/Ox-MPCNP-Cys-PAsp-FA carriers was investigated using the CytoTox96 assay kit. The CytoTox96 assay quantitatively measures LDH, a stable cytosolic enzyme released upon cell lysis. LDH is an oxidoreductase enzyme that catalysis the inter-conversion of pyruvate and lactate. Fifty microliters of the control and test samples was added to a 96-well plate, and the same amount of the LDH reagent was added to the wells and then incubated in the dark at room temperature for 30 min. The LDH-releasing amount was measured spectrophotometrically at 490 nm using a multilabel counter (Perkin Elmer, VICTOR3 Multilabel Plate Reader, 1420). Furthermore, the IC<sub>50</sub> concentration was analyzed using the following equation

$$\text{Cell toxicity(\%)} = \frac{\text{OD of the experimental LDH release}}{\text{OD of the maximum LDH release}} \times 100$$

**4.8.3. Cell Morphological Analysis.** The cell morphology changes in 0 h- and 24 h-treated groups were visualized using a CKX41 inverted microscope (Olympus, Wirsam) connected to a camera with getIT software. The cell morphology changes were captured at different time hours (0 and 24 h).

**4.8.4. Cell Apoptosis Analysis (Flow Cytometry Using Annexin V/PI Staining).** Cell apoptosis was detected using an Annexin V/PI staining kit (BD Biosciences, 556547). The Annexin V-FITC and PI assay were used to identify the PS sites on the membrane of apoptotic cells and the cell membrane damage in necrotic cells. The assay was performed according to the manufacturer's instructions and analyzed on the BD Accuri C6 Flow cytometer. Briefly, the Ox-MPCNP-, Ox-MPCNP-Cys-PAsp-FA-, DOX-, and DOX/Ox-MPCNP-Cys-PAsp-FA-treated cells were harvested and resuspended in the 1X binding buffer at a concentration of  $1 \times 10^6$  cells/mL, and 100  $\mu$ L of the cell suspension was transferred into flow cytometry tubes. The cells were further stained with 5  $\mu$ L of both Annexin V-FITC and PI reagents, and the tubes were thoroughly mixed and incubated for 10 min at room temperature in the dark. The apoptotic and necrotic cells were analyzed by flow cytometry within 1 h at a rate of 400 events per second. Data acquisition was carried out until 10,000 events were collected for each sample. Data were further analyzed using BD CSampler software.

**4.8.5. In Vitro Cell-Uptake Studies.** The MCF-7 cells were cultured on a glass coverslip containing a Petri dish and incubated at 37 °C in 5% CO<sub>2</sub> and 85% humidity. Once the cells reach confluency, the cells are further treated with the IC<sub>50</sub> concentration of all the samples for 24 h. After 24 h incubation, the cells were rinsed twice using PBS and 500  $\mu$ L of 4% paraformaldehyde (P6148, Sigma-Aldrich) was added to the cells and incubated for 20 min at 37 °C to fix the cells and then rinsed twice using PBS. For permeabilization, 200  $\mu$ L of 0.2% Triton X-100 (Sigma-Aldrich, T9284) was added to the cells and incubated for 10 min at 37 °C and then rinsed twice using PBS. Pre-warmed staining solution of Mito Tracker 100 nM (M7514, Invitrogen) was added to the cells and incubated for 30 min at 37 °C and then rinsed twice using PBS. For

counterstaining, 300 nM 4',6-diamidino-2-phenylindole (DAPI) was added and incubated for 20 min at 37 °C and then washed twice using PBS. The glass coverslip was taken out and dried for 5 min using Fluoromount Aqueous Mounting Medium (F4680, Sigma-Aldrich); the coverslip was mounted on the glass slide (GLAS4S22M3000F, Lasec) and visualized using a Carl Zeiss live imaging microscope (Axio Observer Z1).

**4.8.6. Statistical Analysis.** The results were accumulated and processed for graphing, and data analysis was done with ANOVA (analysis of variance). All experiments were done in triplicate to monitor the reproducibility of the results, and all data are expressed as the mean  $\pm$  standard deviation.

## ■ ASSOCIATED CONTENT

### Supporting Information

The Supporting Information is available free of charge at <https://pubs.acs.org/doi/10.1021/acsomega.1c04820>.

*In vitro* drug-release studies (PDF)

## ■ AUTHOR INFORMATION

### Corresponding Author

**Mariappan Rajan** – Biomaterials in Medicinal Chemistry Laboratory, Department of Natural Products Chemistry, School of Chemistry, Madurai Kamaraj University, Madurai 625021 Tamil Nadu, India; [orcid.org/0000-0001-9569-8744](https://orcid.org/0000-0001-9569-8744); Phone: +91 9488014084; Email: [rajanm153@gmail.com](mailto:rajanm153@gmail.com); Fax: 0452-2459845

### Authors

**Kandasamy Vinothini** – Biomaterials in Medicinal Chemistry Laboratory, Department of Natural Products Chemistry, School of Chemistry, Madurai Kamaraj University, Madurai 625021 Tamil Nadu, India

**Sathish Sundar Dhilip Kumar** – Laser Research Centre, Faculty of Health Sciences, University of Johannesburg, Johannesburg 2028, South Africa

**Heidi Abrahamse** – Laser Research Centre, Faculty of Health Sciences, University of Johannesburg, Johannesburg 2028, South Africa

Complete contact information is available at:

<https://pubs.acs.org/doi/10.1021/acsomega.1c04820>

### Author Contributions

All authors contributed to analyzing the results and writing the draft and the final version of the article.

### Notes

The authors declare no competing financial interest.

## ■ ACKNOWLEDGMENTS

M.R. appreciates the financial support under the plan of the Science and Engineering Research Board (Ref: EEQ/2020/000201; New Delhi, India) and also acknowledges the PURSE program for the purchase of SEM and FT-IR and UPE programs for the purchase of HR-TEM. K.V. thanks the Council of Scientific and Industrial Research (CSIR), New Delhi, for the Senior Research Fellowship (Ref.no.09/201(0428)/2020-EMR-I).

## ■ REFERENCES

(1) Chen, L.; Zhang, H.; Zheng, J.; Yu, S.; Du, J.; Yang, Y.; Liu, X.; Lin, X. Thermo-sensitively and magnetically ordered mesoporous

carbon nanospheres for targeted controlled drug release and hyperthermia application. *Mater. Sci. Eng., C* **2018**, *84*, 21–31.

(2) Li, X.; Wang, X.; Sha, L.; Wang, D.; Shi, W.; Zhao, Q.; Wang, S. Thermosensitive Lipid Bilayer-Coated Mesoporous Carbon Nanoparticles for Synergistic Thermochemotherapy of Tumor. *ACS Appl. Mater. Interfaces* **2018**, *10*, 19386–19397.

(3) Pradeepkumar, P.; Abdallah Mohamed, E.; Ali Hassan, B.; Mariappan, R. Natural Solvent-Assisted Synthesis of Amphiphilic Copolymeric Nanomicelle for Prolonged Release of Camptothecin Delivery. *New J. Chem.* **2018**, *42*, 10366–10375.

(4) Eleftheriou, K.; Archontia, K.; Katerina, NP.; Zili, S.; Michael, Z.; Jane, A.; Dimitris, T. A. Combination drug delivery system employing thermosensitive liposomes for enhanced cell penetration and improved in-vitro efficacy. *Int. J. Pharm.* **2020**, *574*, 118912.

(5) Vinothini, K.; Naresh Kumar, R.; Andy, R.; Nandhakumar, E.; Mariappan, R. Folate receptor targeted delivery of paclitaxel to breast cancer cells via folic acid conjugated graphene oxide grafted methyl acrylate nanocarrier. *Biomed. Pharmacother.* **2019**, *110*, 906–917.

(6) Li, X.; Kandasamy, V.; Thiyagarajan, R.; Mariappan, R.; Andy, R. Combined photodynamic-chemotherapy investigation of cancer cells using carbon quantum dot-based drug carrier system. *Drug Delivery* **2020**, *27*, 791–804.

(7) Zhang, L.; Peng, W.; Wenfu, Z.; Xingyu, J. Hollow carbon nanospheres for targeted delivery of chemotherapeutics in breast cancer therapy. *J. Mater. Chem. B* **2017**, *5*, 6601.

(8) Wu, W.; Rutian, L.; Xiaochen, B.; Zhenshu, Z.; Dan, D.; Xiaolin, L.; Zhijun, J.; Xiqun, J.; Yiqiao, H. Covalently Combining Carbon Nanotubes with Anticancer Agent: Preparation and Antitumor Activity. *ACS Nano* **2009**, *3*, 2740–2750.

(9) Vinothini, K.; Naresh Kumar, R.; Mariappan, R.; Andy, R.; Najat, M.; Abdallah, M. E. Magnetic Nanoparticles Functionalized Reduced Graphene Oxide-Based Drug Carrier System for Chemo-Photodynamic Cancer. *New J. Chem.* **2020**, *44*, 5265–5277.

(10) Li, L.; Chen, C.; Liu, H.; Fu, C.; Tan, L.; Wang, S.; Fu, S.; Liu, X.; Meng, X.; Liu, H. Multifunctional carbon-silica nanocapsules with gold core for synergistic photothermal and chemo-cancer therapy under the guidance of bimodal imaging. *Adv. Funct. Mater.* **2016**, *26*, 4252–4261.

(11) Zhao, L.; Yuanzhe, L.; Ning, H.; Xian, L.; Hongjian, G.; Xiudan, W.; Yu, C.; Siling, W. Mesoporous carbon nanomaterials in drug delivery and biomedical application. *Drug Delivery* **2017**, *24*, 94–107.

(12) Zhang, L.; Xinglong, Y.; Ying, L.; Wenfu, Z.; Xingyu, J. Hollow carbon nanospheres as a versatile platform for co-delivery of siRNA and chemotherapeutics. *Carbon* **2017**, *121*, 79–89.

(13) Yu, Y.; Kong, L.; Li, L.; Li, N.; Yan, P. Antitumor Activity of Doxorubicin-Loaded Carbon Nanotubes Incorporated Poly (Lactic-Co-Glycolic Acid) Electrospun Composite Nanofibers. *Nanoscale Res. Lett.* **2015**, *10*, 343.

(14) Wang, K.; Hui, Y.; Ying, M.; Yi, W.; Xueying, Y.; Rongqin, H. Specific aptamer-conjugated mesoporous silica-carbon nanoparticles for HER2-targeted chemo-photothermal combined therapy. *Acta Biomater.* **2015**, *16*, 196–205.

(15) Chen, L.; Wei, F.; Xiaojun, Z.; Kexin, Q.; Yingke, M.; Qianqian, Z.; Ming, Q.; Lei, L.; Yanzhong, Z.; Chuanglong, H. Facile synthesis of novel albumin-functionalized flower-like MoS<sub>2</sub> nanoparticles for in vitro chemo-photothermal synergistic therapy. *RSC Adv.* **2016**, *6*, 13040–13049.

(16) Danhier, D.; Olivier, F.; Veronique, P. To exploit the tumor microenvironment: Passive and active tumor targeting of nanocarriers for anticancer drug delivery. *J. Controlled Release* **2010**, *148*, 135–146.

(17) Yang, P.; Ye, T.; Yongzhi, M.; Ranran, G.; Haibao, P.; Qin, J.; Wuli, Y. Metal-Organic Frameworks-Derived Carbon Nanoparticles for Photoacoustic Imaging-Guided Photothermal/Photodynamic Combined Therapy. *ACS Appl. Mater. Interfaces* **2018**, *10*, 42039–42049.

(18) Yu, W.; Rui, L.; Yang, Z.; Huile, G. Size-Tunable Strategies for a Tumor Targeted Drug Delivery System. *ACS Cent. Sci.* **2020**, *6*, 100–116.

(19) El-Zahed, M. M.; Zakaria, AB.; Mohamed, I. AD.; Ahmed, K. E. S.; Magy, M. A.; Ayman, H. In vivo toxicity and antitumor activity of newly green synthesized reduced graphene oxide/silver nanocomposites. *Bioresour. Bioprocess* **2021**, *8*, 44.

(20) Pei, X.; Zhou, Z.; Zhoujie, G.; Junyu, C.; Xin, Z.; Xinting, C.; Wan, Q.; Wang, J. PEGylated nano-graphene oxide as a nanocarrier for delivering mixed anticancer drugs to improve anticancer activity. *Sci. Rep.* **2020**, *10*, 2717.

(21) Zhang, P.; Huailin, Y.; Wei, S.; Wanguo, L.; Li, C.; Chunsheng, X. Hypoxia-Responsive Polypeptide Nanoparticles Loaded with Doxorubicin for Breast Cancer Therapy. *ACS Biomater. Sci. Eng.* **2020**, *6*, 2167–2174.

(22) Yao, Y.; Phei Er, S.; Yan, N.; Ping-Pui, W.; Linjia, J.; Xiaojing, Y.; Jun, C.; Tao, D.; Liang, X.; Herui, Y.; Hai, H.; Xiaoding, X. Multifunctional sharp pH-responsive nanoparticles for targeted drug delivery and effective breast cancer therapy. *J. Mater. Chem. B* **2019**, *7*, 576–585.

(23) Shi, Y.; Roy van der, M.; Xiaoyuan, C.; Twan, L. The EPR effect and beyond: Strategies to improve tumor targeting and cancer nanomedicine treatment efficacy. *Theranostics* **2020**, *10*, 7921–7924.

(24) Pradeepkumar, P.; Naresh Kumar, R.; Abdullah, A.; Murugan, A.; Mariappan, R. Deep Eutectic Solvent-Mediated FA-g-β-Alanine-co-PCL Drug Carrier for Sustainable and Site-Specific Drug Delivery. *ACS Appl. Bio Mater.* **2018**, *1*, 2094–2109.

(25) Deshpande, N. U.; Manickam, J. Biotin-Tagged Polysaccharide Vesicular Nanocarriers for Receptor-Mediated Anticancer Drug Delivery in Cancer Cells. *Biomacromolecules* **2018**, *19*, 3572–3585.

(26) Franks, S. J.; Kate, F.; Rita, F.; Katherine, MH.; Richard, JW.; Ross, DH.; David, R. N. Harnessing the self-assembly of peptides for the targeted delivery of anticancer agents. *Mater. Horiz.* **2020**, *7*, 1996–2010.

(27) Fei, Y.; Menghuan, L.; Yanan, L.; Xua, W.; Chencheng, X.; Zuosu, W.; Jiaying, X.; Zilu, X.; Kai-Yong, C.; Zhong, L. Hierarchical integration of degradable mesoporous silica nano reservoirs and supramolecular dendrimer complex as a general-purpose tumor-targeted biomimetic nanoplatform for gene/small-molecule anticancer drug co-delivery. *Nanoscale* **2020**, *12*, 16102–16112.

(28) Maji, T.; Sanjib, B.; Jaynaseni, B.; Tarun, K.; Mandal. Dual-stimuli-responsive l-serine-based zwitterionic UCST-type polymer with tunable thermosensitivity. *Macromolecules* **2015**, *48*, 4957–4966.

(29) Lee, E. S.; Kyung Taek, O.; Dongin, K.; Yu Seok, Y.; You Han, B. Tumor pH-responsive flower-like micelles of poly (l-lactic acid)-b-poly (ethylene glycol)-b-poly(l-histidine). *J. Controlled Release* **2007**, *123*, 19–26.

(30) Raza, A.; Uzma, H.; Tahir, R.; Muhammad, B.; Hafiz, M. N. I. “Smart” materials-based near-infrared light-responsive drug delivery systems for cancer treatment: A review. *J. Mater. Res. Technol.* **2019**, *8*, 1497–1509.

(31) Shahriari, M.; Mahsa, Z.; Khalil, A.; Seyed Mohammad, T.; Mohammad, R.; Mona, A. Enzyme responsive drug delivery systems in cancer treatment. *J. Controlled Release* **2019**, *308*, 172–189.

(32) Mo, R.; Gu, Z. Tumor microenvironment and intracellular signal-activated nanomaterials for anticancer drug delivery. *Mater. Today* **2016**, *19*, 274–283.

(33) Wang, Y.; Yu, C.; Yating, Z.; Bing, H.; Xiaoli, S.; Donghua, D.; Qiang, Z.; Siling, W. Fluorescent carbon dot-gated multifunctional mesoporous silica nanocarriers for redox/enzyme dual-responsive targeted and controlled drug delivery and real-time bioimaging. *Eur. J. Pharm. Biopharm.* **2017**, *117*, 105–115.

(34) Li, W.; Pomchol, H.; Yang, C.; Yuliang, G.; Dan, L.; Ying, W.; Yan, Y.; Maoquan, C. Drug-Loaded Polymer-Coated Graphitic Carbon Nanocages for Highly Efficient in Vivo Near-Infrared Laser-Induced Synergistic Therapy through Enhancing Initial Temperature. *ACS Appl. Mater. Interfaces* **2018**, *10*, 31186–31197.

(35) Li, X.; Yan, Y.; Lin, Y.; Jiao, J.; Wang, D.; Di, D.; Zhang, Y.; Jiang, T.; Zhao, Q.; Wang, S. Hollow mesoporous carbon as a near-infrared absorbing carrier compared with mesoporous carbon nanoparticles for chemo-photothermal therapy. *J. Colloid Interface Sci.* **2017**, *494*, 159–169.

- (36) Wu, F.; Ming, Z.; Hanwen, L.; Dong, L.; Yaliang, H.; Yonghong, X.; Yuqing, H.; Shengqiang, H.; Jianxiu, W.; Xinyao, Y.; Jun, Z. Triple Stimuli-Responsive Magnetic Hollow Porous Carbon-Based Nanodrug Delivery System for Magnetic Resonance Imaging-Guided Synergistic Photothermal/Chemotherapy of Cancer. *ACS Appl. Mater. Interfaces* **2018**, *10*, 21939–21949.
- (37) Mauro, N.; Cinzia, S.; Simonpietro, A.; Gennara, C.; Gaetano, G. Folic acid-functionalized graphene oxide nanosheets via plasma etching as a platform to combine NIR anticancer phototherapy and targeted drug delivery. *Mater. Sci. Eng., C* **2020**, *107*, 110201.
- (38) Pradeepkumar, P.; Dharman, G.; Murugaraj, J.; Murugan, A. M.; Mariappan, R. Assembling of multifunctional latex-based hybrid nanocarriers from *Calotropis gigantea* for sustained (doxorubicin) DOX releases. *Biomed. Pharmacother.* **2017**, *87*, 461–470.
- (39) Wang, H.; Xiangui, L.; Zhiqiang, M.; Dan, W.; Linzhao, W.; Jieqiong, Z.; Lan, S.; Feng, Y. Hydrophilic mesoporous carbon nanospheres with high drug-loading efficiency for doxorubicin delivery and cancer therapy. *Int. J. Nanomed.* **2016**, *11*, 1793–1806.
- (40) Zhang, Y.; Lu, H.; Lin, L. H.; Yan, Q. C.; Rong, H. H.; Ming, L. C.; Yang, S.; Jian, H. W. Mesoporous Carbon nanoparticles capped with polyacrylic acid as drug carrier for bi-trigger continuous drug release. *J. Mater. Chem. B* **2016**, *4*, 5178.
- (41) Nasrollahi, F.; Jaleh, V.; Abbas, A. K.; Sierin, L.; Ali Jahanian, N. Targeted Delivery of Docetaxel by Use of Transferrin/Poly (allylamine hydrochloride)-functionalized Graphene Oxide Nanocarrier. *ACS Appl. Mater. Interfaces* **2016**, *8*, 13282–13293.
- (42) Xu, G.; Shengju, L.; Huan, N.; Wenping, L.; Ren'an, W. Functionalized mesoporous carbon nanoparticles for targeted chemophotothermal therapy of cancer cells under near-infrared irradiation. *RSC Adv.* **2014**, *4*, 33986.
- (43) Wang, X.; Qian, L.; Hongyan, P.; Shuangzhu, J.; Hong, W.; Yongyong, S.; Zhuhua, W. Oxidation modification of chitosan-based mesoporous carbon by soft template method and the adsorption and release properties of hydroxycamptothecin. *Sci. Rep.* **2020**, *10*, 15772.
- (44) Zhang, Z.; Xinyu, W.; Binbin, L.; Yuanjing, H.; Zhengwei, C.; Jing, Y.; Yi, L. Paclitaxel-loaded PLGA microspheres with a novel morphology to facilitate drug delivery and antitumor efficiency. *RSC Adv.* **2018**, *8*, 3274.
- (45) Li, C.; Ying, M.; Shanshan, W.; Min, Q.; Jianxin, W.; Weiyue, L.; Rongqin, H. Mesoporous Carbon Nanospheres Featured Fluorescent Aptasensor for Multiple Diagnosis of Cancer in Vitro and in Vivo. *ACS Nano* **2015**, *9*, 12096–12103.
- (46) Wang, Y.; Kaiyuan, W.; Ren, Z.; Xingang, L.; Xueying, Y.; Jianxin, W.; Ernst, W.; Rongqin, H. Synthesis of Core-Shell Graphitic Carbon@Silica Nanospheres with Dual-Ordered Mesopores for Cancer-Targeted Photothermochemotherapy. *ACS Nano* **2014**, *8*, 7870–7879.
- (47) ud Din, F.; Waqar, A.; Izhar, U.; Omer Salman, Q.; Omer, M.; Shumaila, S.; Alam, Z. Effective use of nanocarriers as drug delivery systems for the treatment of selected tumors. *Int. J. Nanomed.* **2017**, *12*, 7291–7309.
- (48) Zhang, F.; Meng, X.; Yongwei, Z.; Yanan, Z.; Mei, L.; Na, Y.; Tongtong, D.; Mingmei, Z.; Jimin, X. Chitosan and dextran stabilized GO-iron oxide nanosheets with high dispersibility for chemotherapy and photothermal ablation. *Ceram. Int.* **2019**, *45*, 5996–6003.
- (49) Liu, X.; Zheng, J.; Tingting, S.; Minghong, W.; Haijiao, Z. Surfactant-assisted selective etching strategy for generation of rattle-like mesoporous silica nanoparticles. *J. Colloid Interface Sci.* **2017**, *490*, 497–504.
- (50) Zhou, L.; Kai, D.; Zhaowei, C.; Jinsong, R.; Xiaogang, Qu. Near-infrared absorbing mesoporous carbon nanoparticle as an intelligent drug carrier for dual-triggered synergistic cancer therapy. *Carbon* **2015**, *82*, 479–488.
- (51) Gui, X.; Yang, C.; Zheyu, Z.; Longfei, L.; Fangliang, Z.; Wenxuan, Y.; Yuliang, G.; Maoquan, C. Fluorescent hollow mesoporous carbon spheres for drug loading and tumor treatment through 980-nm laser and microwave co-irradiation. *Biomaterials* **2020**, *248*, 120009.
- (52) Gou, X.; Yuan, C.; Xiaotian, Z.; Yanli, L.; Jianjun, C.; Wei, E. Y. Advances in redox-responsive drug delivery systems of tumor microenvironment. *J. Nanobiotechnol.* **2018**, *16*, 74.
- (53) Li, M.; Song, W.; Tang, Z.; Lv, S.; Lin, L.; Sun, H.; Li, Q.; Yang, Y.; Hong, H.; Chen, X. Nanoscaled Poly (l-glutamic acid)/Doxorubicin-Amphiphile Complex as pH-responsive Drug Delivery System for Effective Treatment of Non-small Cell Lung Cancer. *ACS Appl. Mater. Interfaces* **2013**, *5*, 1781–1792.
- (54) Wang, H.; Yubing, S.; Jinhui, Yi.; Jianping, F.; Jing, D.; Alejandra del, C. A.; Shuiqin, Z. Fluorescent porous carbon nanocapsules for two-photon imaging, NIR/pH dual-responsive drug carrier, and photothermal therapy. *Biomaterials* **2015**, *53*, 117–126.
- (55) Mohammed Albayati, S. H.; Pervin, D. pH and GSH dual responsive smart silica nanocarrier for doxorubicin delivery. *Mater. Res. Express* **2019**, *6*, 065705.
- (56) Zhang, J.; Xian, J.; Xiang, W.; Qian, X.; Hao, Z.; Yuxing, Z.; Min, L.; Zuyong, W.; Xuefeng, H.; Yunbing, W. Bio-responsive smart polymers and biomedical applications. *J. Phys. Mater.* **2019**, *2*, 032004.
- (57) Yassemi, A.; Soheila, K.; Hossein, Z. Folic acid receptor-targeted solid lipid nanoparticles to enhance cytotoxicity of letrozole through induction of caspase dependent apoptosis for breast cancer treatment. *Pharm. Dev. Technol.* **2020**, *25*, 397–407.
- (58) Zhang, S.-Q.; Xun, L.; Qi-Xuan, S.; Omar, J.; Ting, Y.; Ming-Li, C.; Jian-Hua, W.; Wei, C. CuS@PDA-FA nanocomposites: a dualstimuli responsive DOX delivery vehicle with ultrahigh loading level for synergistic photothermal-chemotherapies on breast cancer. *J. Mater. Chem. B* **2020**, *8*, 1396–1404.
- (59) Akbarzadeh, I.; Mohammad Tavakkoli, Y.; Saeedeh, A.; Mohsen, C.; Dariush, N. Folic acid-functionalized niosomal nanoparticles for selective dual-drug delivery into breast cancer cells: An in-vitro investigation. *Adv. Powder Technol.* **2020**, *31*, 4064–4071.
- (60) Zhao, J.; Delong, Z.; Yuedan, L.; Yi, L.; Shengbin, J.; Xiaoling, L.; Tianfeng, C. Selenadiazole Derivatives Antagonize Hyperglycemia-Induced Drug Resistance in Breast Cancer Cells by Activation of AMPK Pathway. *Metallomics* **2017**, *9*, 535–545.